Ⓔ

Estimation of the Orientations of the S-net Cabled Ocean-Bottom Sensors

by Ryota Takagi, Naoki Uchida, Takashi Nakayama, Ryosuke Azuma, Akira Ishigami, Tomomi Okada, Takeshi Nakamura, and Katsuhiko Shiomi

ABSTRACT

The Seafloor Observation Network for Earthquakes and Tsunamis along the Japan Trench (S-net) is a novel cabled ocean-bottom station network covering a broad offshore region east of northeastern Japan. To best use the S-net data, we estimated sensor orientations of all 150 S-net stations, because without this information the orientations of measurements in geodetical coordinates cannot be specified. We determined three parameters of the sensor orientation at each station: the tilt angle of the long axis of the cable, the rotation angle around the long axis, and the azimuth of the long axis. We estimated the tilt and rotation angles by using the direct current components of accelerometers recording the gravitational acceleration. The tilt and rotation angles slightly varied within the range of 0.001°–0.1° for most stations during the period from 2016 to 2018 except for coseismic steps of rotation angles greater than 1° because of the 20 August 2016 M_w 6.0 off Sanriku and 20 November 2016 M_w 6.9 off Fukushima earthquakes. The long-axis azimuths were estimated by the particle motions of long-period Rayleigh waves. We used the accelerometer records in 0.01–0.03 Hz of 7–14 teleseismic earthquakes with M_w 7.0–8.2. The azimuths were constrained with 95% confidence intervals of ±3°–12°. After correcting original waveforms based on the estimated sensor orientation, we confirmed coherent waveforms within the whole S-net stations and separation of Rayleigh and Love waves in radial and transverse components. The waveforms were also coherent with those of on-land broadband stations. We provide the estimated sensor orientations and rotation matrix for conversion from the XYZ to east, north, and up components. The estimated orientation can be a fundamental resource for further seismic and geodetic explorations based on S-net data.

Supplemental Content: Tables of estimated sensor orientations and of the rotation matrix for converting XYZ to east, north, and up (ENU) components, and figure showing the sensor azimuths estimated from Rayleigh and *P*-wave polarizations.

INTRODUCTION

The northeast Japan subduction zone is seismically active and is among the most studied subduction zones in the world. In this region, the Seafloor Observation Network for Earthquakes and Tsunamis along the Japan Trench (S-net) was installed by the National Research Institute for Earth Science and Disaster Resilience (NIED) following the 2011 M_w 9.0 Tohoku-oki earthquake. The deployment of the cable system begun in 2013 was completed in 2017; the data have been publicly available since October 2018 on the NIED's webpage (see Data and Resources; National Research Institute for Earth Science and Disaster Resilience, 2019b). The new data can possibly not only greatly improve our knowledge regarding various aspects of solid earth science including subsurface structure, regular earthquakes, and slow earthquakes but also show unknown phenomena of the earth system beneath the offshore region along the Japan trench.

S-net consists of 150 cabled ocean-bottom stations (Kanazawa *et al.*, 2016; Mochizuki *et al.*, 2016; Uehira *et al.*, 2016; Fig. 1a). The 150 stations cover the offshore region of the northeast Japan subduction zone within 300 km of the coast and for 1000 km along the Japan and Kuril trenches. The station separation is approximately 30 km in the direction perpendicular to the trench and approximately 50–60 km along the trench. The ocean depth range of the S-net stations is 102–7830 m. Stations shallower than 1500 m are routed within grooves approximately 1 m below the seafloor to avoid fishery activities.

Each S-net station consists of a geophone (velocity seismometer), strong-motion accelerometer, high- and low-sensitivity accelerometer, tilt meter, and water pressure gauge for seismic, geodetic, tsunami, and acoustic observations (Kanazawa *et al.*, 2016; Mochizuki *et al.*, 2016; Uehira *et al.*, 2016). The geophone and accelerometers have three orthogonal components (X, Y, and Z) in a right-handed coordinate system. Although pop-up type ocean-bottom seismometers typically have a gimbal system to maintain a vertical position,

doi: 10.1785/0220190093

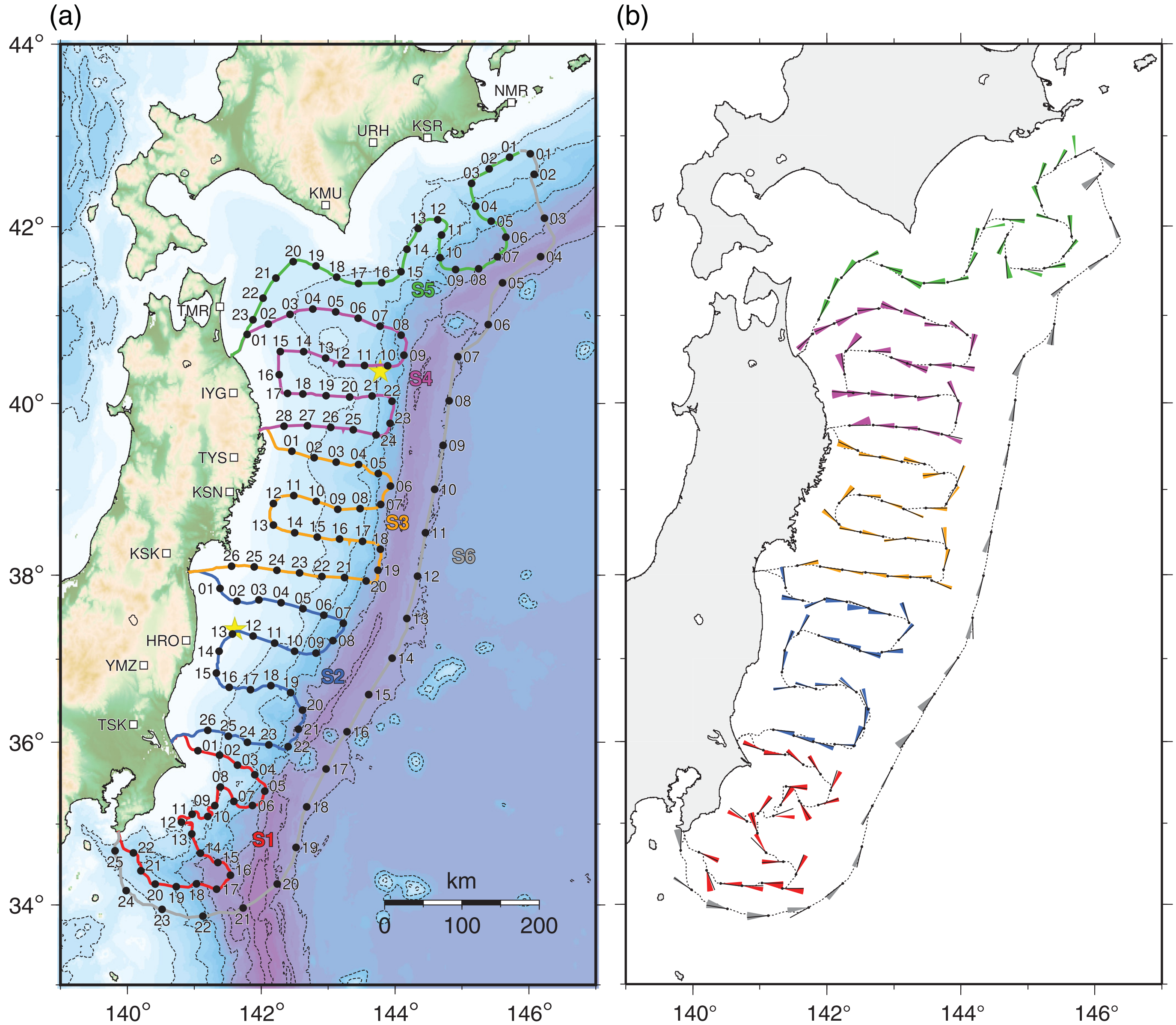

▲ **Figure 1.** (a) Map of S-net. The colored lines show the six cable systems (S1–S6). The black dots indicate the locations of all stations. The associated numbers are the station numbers within each cable line. The station names are composed of the cable number and the station number of the cable (e.g., N.S1N01). The white squares show the locations of the F-net stations used. The two yellow stars represent the epicenters of the two earthquakes: the 20 August 2016 M_w 6.0 off-Sanriku earthquake (northern one) and the 22 November 2016 M_w 6.9 off-Fukushima earthquake (southern one). The dashed contour shows the ocean depth at 1500 m intervals. (b) Sensor azimuths estimated by this study. The colored wiggles show the 95% confidence intervals of the estimated azimuth. The black bars indicate the azimuths of the cable route data.

the S-net sensors are fixed on cables for long-term stability (Fig. 2). The X component is set parallel, and the Y and Z components are set perpendicular to the cable's long axis (Kanazawa, 2013; Aoi, 2016).

Although the X axis is parallel to the cable route, the cable installation situation on the seafloor has not been confirmed. Thus, the actual sensor orientations on the seafloor are unknown. However, it is necessary to know the orientation of each S-net sensor for detailed seismic or geodetic analyses. The purpose of this study was to estimate the sensor orientations of S-net and provide information for further data analyses based on the S-net data.

We define sensor orientation using three parameters: azimuth, tilt angle, and rotation angle (Fig. 2). The azimuth, tilt, and rotation are also termed the yaw, pitch, and roll angles, respectively. When all the angles are zero, XYZ axes are identical to east, north, and up (ENU) axes. All the angles are defined as anticlockwise angles around the rotation axes.

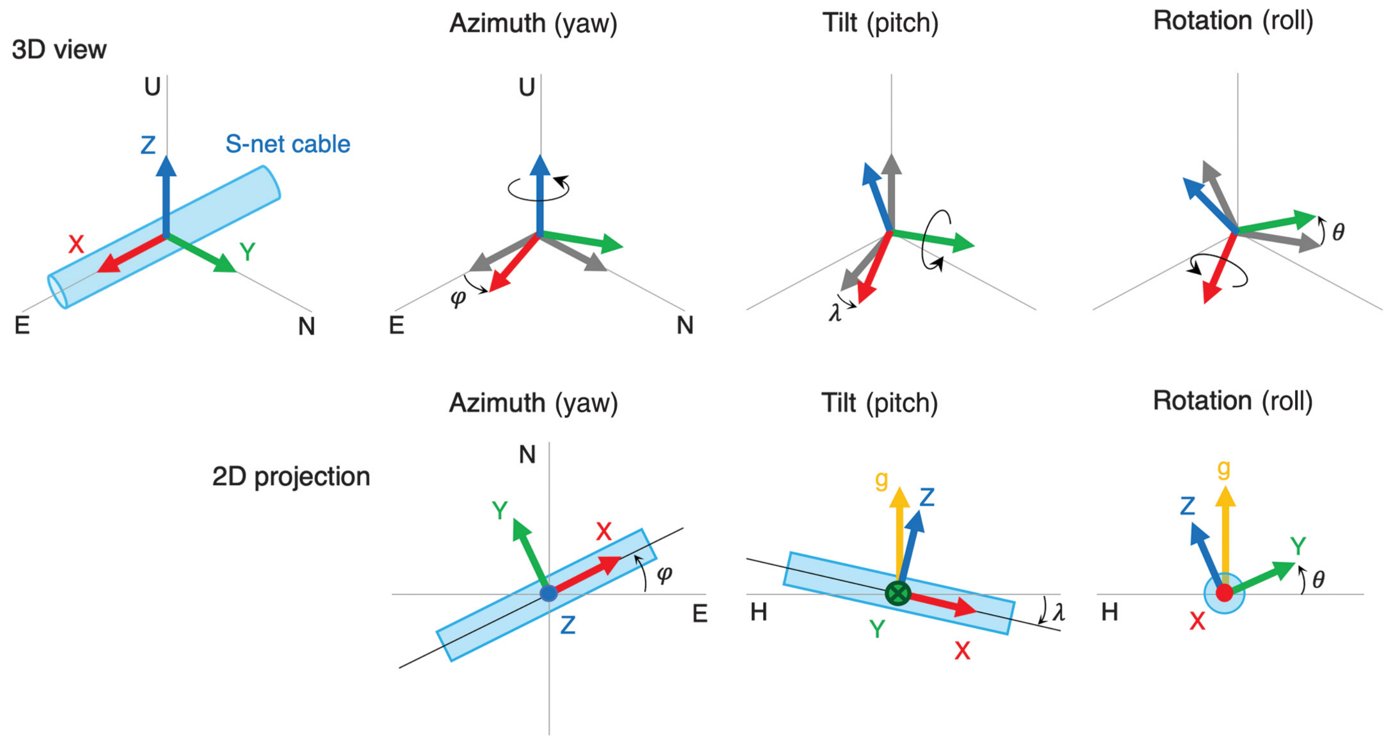

▲ **Figure 2.** Schematic of the definition of the sensor orientations. The X component is parallel to the long axis of the cable. The Y and Z components are perpendicular to the cable long axis. U, N, E, and H denote the up, north, east, and horizontal directions. The orange arrows (g) represent the reaction force of gravity, which acts on the accelerometer. Note we define the sensor azimuth as an anti-clockwise angle from the east direction.

The azimuth is the horizontal angle of the X axis (cable's long axis) from east. The tilt angle is the dip angle of the X axis. The rotation angle is the angle around the X axis. The rotation angle is zero when the Y axis is in the horizontal plane.

Here, we first estimated the tilt and rotation angles from the direct current (DC) components of the accelerometer. Then, we estimated the azimuth of the X axis using the polarization of long-period teleseismic Rayleigh waves. Finally, we compared the corrected seismograms of S-net to those of the on-land broadband seismograms of the Full Range Seismograph Network of Japan (NIED F-net; see Data and Resources; National Research Institute for Earth Science and Disaster Resilience, 2019a).

TILT AND ROTATION

Data and Methods

Each S-net station is equipped with servo accelerometers, JA5-typeIII-A (Japan Aviation Electronics Industry, Ltd), as strong-motion sensors. The accelerometers have sensitivity to the DC components and record the acceleration of the reaction force of gravity. Thus, the DC offsets of acceleration records provide a vertical upward direction. We used the DC offsets of the strong-motion accelerometer installed in S-net to estimate the tilt and rotation angles of the S-net sensors as follows:

$$g = \sqrt{x^2 + y^2 + z^2}, \quad (1)$$

$$\lambda = \arcsin(-x/g), \quad (2)$$

$$\theta = \arctan(y/z), \quad (3)$$

in which x, y, and z are the DC offsets of the X, Y, and Z components, respectively, and g, λ, and θ are the gravitational acceleration, tilt, and rotation angles, respectively (Fig. 2). The DC offsets are estimated by the mean values of acceleration records. The time windows for the mean depends on the dataset as described subsequently.

We examined the tilt and rotation angles using two datasets: event-triggered data and continuous data. The event-triggered data were used to examine coseismic changes of tilt and rotation angles. Nakamura and Hayashimoto (2019) reported strong ground motions cause changes in tilt and rotation angles of a cabled ocean-bottom seismic network similar to S-net. The continuous data were used to investigate long-term temporal variations in the tilt and rotation angles.

For the event-triggered data analysis, we used Japan Meteorological Agency (JMA)'s unified earthquake catalog, which is mainly based on on-land permanent stations (see Data and Resources). We selected 949 earthquakes with an

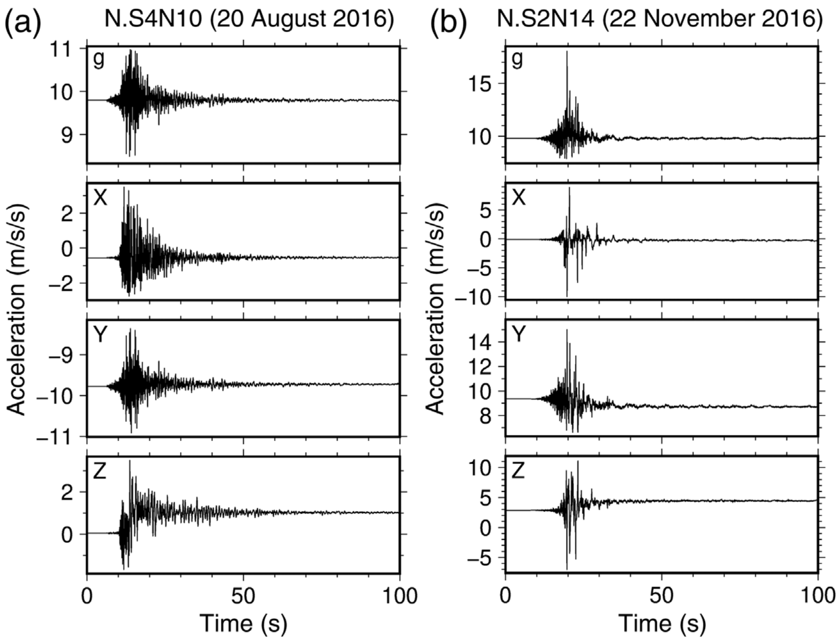

▲ **Figure 3.** (a) Raw acceleration seismograms of the 20 August 2016 M_w 6.0 off-Sanriku earthquake at station N.S4N10. The time zero indicates the origin time. (b) Raw acceleration seismograms of the 22 November 2016 M_w 6.9 off-Fukushima earthquake at station N.S2N14.

$M_{JMA} \geq 4.0$ from 15 August 2016 to 31 December 2018 in and around the network (33°–44° N, 139°–147° E, the same area with Fig. 1). Earthquakes within a 200 km radius were used for the analysis of each station. The DC offsets in the X, Y, and Z components were estimated by the mean values of X, Y, and Z components, respectively, within two time windows: $T_P - 60 \leq t \leq T_P - 10$ and $T_S + 100 \leq t \leq T_S + 150$, in which t is the time in seconds and T_P and T_S are the arrival times of P and S waves, respectively. The travel times of the P and S waves were computed using a regional 1D velocity model (Hasegawa *et al.*, 1978). We then computed the tilt and rotation angles using equations (1)–(3) and determined the difference between the angles in the two time windows. We also calculated the peak ground acceleration (PGA) within $T_P - 10 \leq t \leq T_S + 100$. To remove overlapping events, we did not use waveforms when the maximum acceleration within the time windows for the DC offset estimation was greater than the PGA.

For the continuous data, we estimated the daily tilt and rotation angles of each station. We first calculated tilt and rotation angles from the mean values of 1 min records in the X, Y, and Z components. We then calculated daily averages of tilt and rotation angles from the 1440 1 min data. We used the inverse of the variances in the gravitational acceleration in the 1 min records as a weighting factor for the daily averages. The variances in the gravitational acceleration for the 1 min records δ_g^2 were calculated by the law of error propagation as follows:

$$\delta_g^2 = \frac{x^2\delta_x^2 + y^2\delta_y^2 + z^2\delta_z^2}{x^2 + y^2 + z^2}, \tag{4}$$

in which δ_x^2, δ_y^2, and δ_z^2 are the variance in the X, Y, and Z components, respectively, of the 1 min records. The weighted average largely decreases the contamination by earthquakes and outliers that are included in raw data. We also employed threshold values for gravitational acceleration and used the 1 min data within $9.60\ (\mathrm{m/s^2}) \leq g \leq 10.0\ (\mathrm{m/s^2})$.

The resolution of S-net strong-motion accelerometer is 9×10^{-6} m/s/s approximately. Thus, the resolution of tilt and rotation angles is 9×10^{-7} radian (5×10^{-5} degrees) approximately, which is estimated by dividing the accelerometer resolution by the gravitational acceleration. Because this estimation is for one data point, the effective resolution is reduced by the factor of square root of the number of data points for averaging.

Results and Discussion

Figure 3 shows examples of coseismic changes in the tilt and rotation angles because of two earthquakes: the 20 August 2016 M_w 6.0 (M_{JMA} 6.4) off-Sanriku and the 22 November 2016 M_w 6.9 (M_{JMA} 7.4) off-Fukushima earthquakes. Although the DC offsets of the gravitational acceleration and X (cable's long axis) component waveforms show limited changes before and after the main phase arrival, the DC offsets of the Y and Z components perpendicular to the cable's long axis clearly shifted following the main phase arrival. The resultant changes in the tilt and rotation angles at N.S4N10 by the M_w 6.0 off-Sanriku earthquake were −0.07° and 5.72°, respectively. The tilt and rotation angle changes at N.S2N14 by the M_w 6.9 off-Fukushima earthquake were 1.08° and 9.95°, respectively. In total, we observed coseismic changes in the tilt and rotation angles greater than 1° only at one station (N.S4N10) as a result of the 2016 off-Sanriku earthquake and only at three stations (N.S2N13, N.S2N14, and N.S2N15) as a result of the 2016 off-Fukushima earthquake. No other earthquakes caused changes in the tilt and rotation angles of greater than 1°.

Figures 4a,b show the relationship between the PGA and coseismic changes in the tilt and rotation angles. The tilt and rotation angle changes increase as the PGA increases, particularly within a range larger than approximately 10^{-2} to 10^{-1} m/s/s. This correlation is consistent with the results of a similar cabled ocean-bottom station (Nakamura and Hayashimoto, 2019) and suggests that strong ground motion causes changes in sensor orientation. In the PGA range, the rotation angle changes tend to be 3–5 times larger than the tilt angle change. Figure 4c shows the histogram of tilt and rotation angle changes within a PGA range 0.1–0.13 m/s/s. Because the number of angle change data is large, the difference between the mean values of tilt and rotation changes is statistically significant. The larger changes in rotation angles can be inferred from the larger changes in the Y and Z components than those in the X components shown in Figure 3. The results suggest that the cylindrical shape of the S-net cable

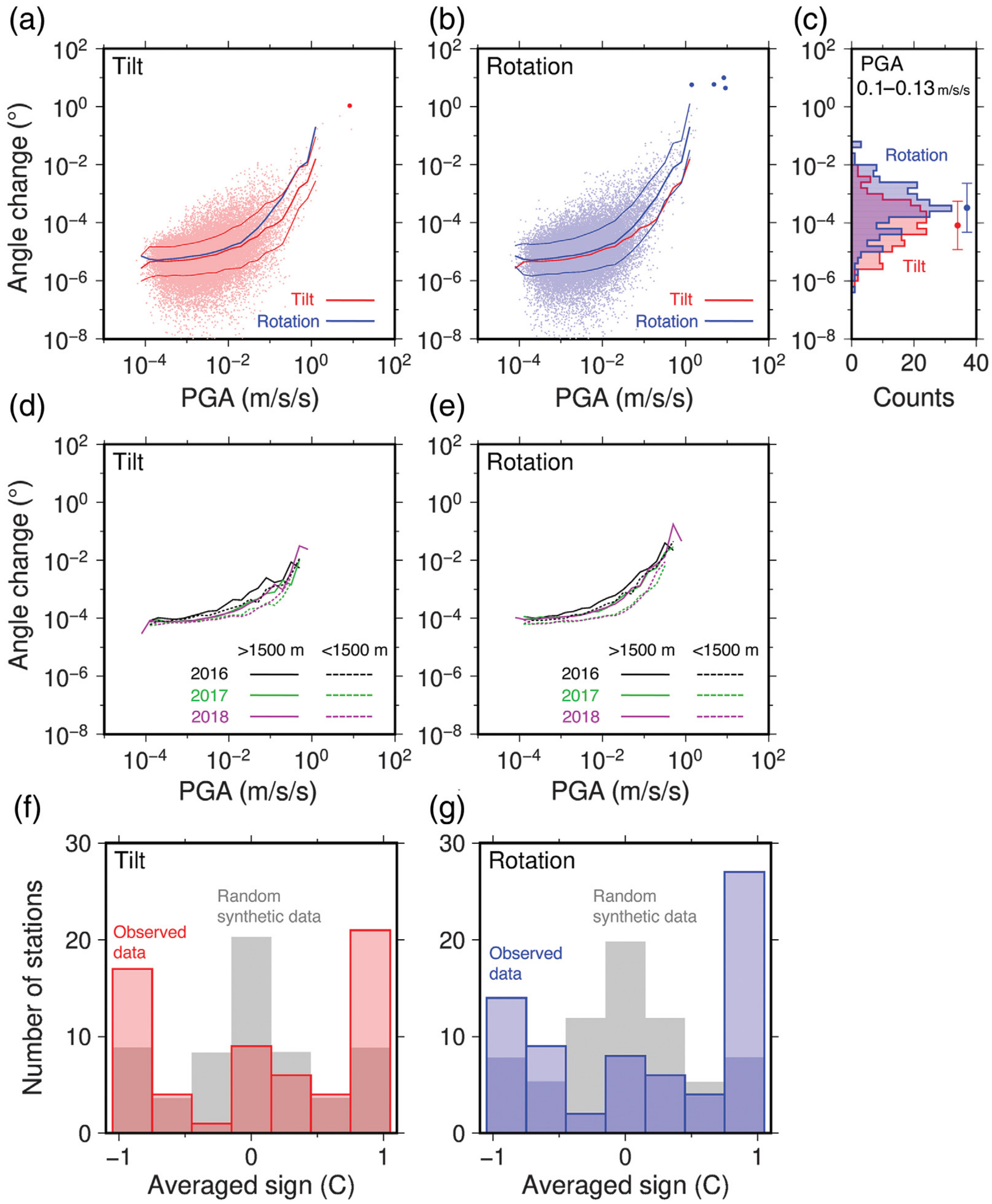

▲ **Figure 4.** (a) Relationship between the peak ground acceleration (PGA) and change in tilt angle. The small light red dots show individual measurements. The large red dot shows a tilt change greater than 1° at N.S2N14 on 22 November 2016. The thick and thin red curves show the average and standard deviation, respectively, of the tilt angle changes. Note that we computed the average and standard deviation after taking logarithm of original data. The blue curve is the average of the rotation angle changes identical to the blue curve in (b). (b) Relationship between the PGA and change in rotation angle. The small light blue dots show individual measurements. The large blue dot shows rotation changes greater than 1° resulting from the two earthquakes on 20 August and 22 November 2016. The thick and thin blue curves show the average and standard deviation, respectively, of the rotation angle changes. The red curve is the average of tilt angle changes identical to the red curve in (a). (c) Histograms of tilt (red) and rotation (blue) angle changes for the PGA range in 0.1–0.13 m/s/s. The dots and error bars represent the averages and standard deviations. (d) Averages of tilt angle changes determined from three time periods: 2016 (black), 2017 (green), and 2018 (pink). The solid and dashed curves show the results for stations shallower and deeper than 1500 m, respectively. (e) Same as (d), but for the rotation angle change. (f) Number of stations with respect to the averaged sign C of the tilt changes. The red and gray histograms were created from observed data and synthetic data with randomly changed tilt angles, respectively. The averaged sign C is defined by equation (5) and indicates the consistency of the direction of tilt and rotation changes over two or more earthquakes. When the tilt always changes in the same direction C becomes 1 or −1. When the tilt randomly changes in both positive and negative directions, C becomes 0. (g) Number of stations with respect to the averaged sign C of the rotation changes. The blue and gray histograms were created from observed data and synthetic data with randomly changed rotation angles, respectively.

more easily allows for changes in the rotation angle than changes in the tilt angle.

A possible mechanism for the changes in tilt and rotation angles is a reduction in the coupling between S-net cable and ocean bottom because of strong ground motion allowing the cable to move to release the twist and bending strain in the cable that is produced at the time of deployment (Nakamura and Hayashimoto, 2019). If this is the case, the magnitude of the coseismic angle changes may gradually decrease over time as the coupling increases and the strain decreases. In addition, if the coseismic changes are related to the cable strain, the tilt and rotation angles may always change in the same directions over more than two earthquakes.

Figure 4d,e shows the relationship between the PGA and tilt and rotation angle changes for the three time periods of 2016, 2017, and 2018. The mean values of the tilt and rotation angle changes during 2016 are larger than those during 2017 and 2018. The difference in the mean values is statistically significant in the PGA range from approximately 10^{-3} to 10^{-1} m/s/s. Thus, the magnitude of the coseismic changes tends to decrease over time, which is the trend expected by the aforementioned mechanism. Within the PGA range larger than 10^{-1} m/s/s, the tilt and rotation angle changes do not seem to significantly depend on the time period, suggesting that a strong motion larger than 10^{-1} m/s/s might surmount the coupling increase over time.

To check the directionality of the tilt and rotation angle changes, we defined the averaged sign C of the tilt angle changes to indicate consistency in the tilt change directions over two or more earthquakes as follows:

$$C = \frac{1}{N} \sum_{i=1}^{N} \frac{\Delta\lambda_i}{|\Delta\lambda_i|}, \tag{5}$$

in which $\Delta\lambda_i$ is the tilt angle change caused by the ith earthquake and N is the number of earthquakes. We also defined the averaged sign C for the rotation angle change in the same manner. Here, we used stations that observed a PGA greater than 10^{-1} m/s/s and tilt and rotation angle changes greater than 10^{-4} degrees for two or more earthquakes. The total number of stations that satisfy the criterion is 62 for tilt change and 71 for rotation change. The number of earthquakes N that are used to compute C for each station is limited. For tilt, $N = 2$ at 24 stations, $N = 3$ at 16 stations, $N = 4$ at 12 stations, $5 \le N \le 9$ at 6 stations, and $N \ge 10$ at 4 stations. For rotation, $N = 2$ at 17 stations, $N = 3$ at 19 stations, $N = 4$ at 14 stations, $5 \le N \le 9$ at 15 stations, and $N \ge 10$ at 6 stations.

We also examined C for synthetic data with randomly changed angles. At first, for each station, we randomly changed the signs of observed angle changes with retaining the number of earthquakes N and computed the averaged sign C. Then, we aggregated C for all stations and created a histogram of C. We repeated the previous procedure by changing random numbers and created 10,000 histograms of C. Finally, we computed the mean of the 10,000 histograms to show the average characteristics of C for random dataset. Because the number of earthquakes for each station is limited, C for random data also can be $+1$ or -1. In the case of $N = 2$, for example, C can be $+1$ with 25% chance, -1 with 25% chance, and 0 with 50% chance if the angle changes are random.

Figure 4f,g shows the number of stations with respect to C of the tilt and rotation angle changes. The number of stations with C close to -1 and 1 are greater than that of the randomly changed data. In contrast, the number of stations with C around 0 is smaller than that of the randomly changed data. This result suggests that most stations tended to rotate in the same direction over two or more earthquakes.

The coupling should also depend on the installation situation of the cables. Figure 4d,e also shows the relationship between the PGA and tilt and rotation angle changes for two station groups: the stations shallower than 1500 m, and the stations deeper than 1500 m. The cables of the shallow stations are routed within grooves. The changes in the tilt and rotation angles are smaller at the shallow stations than those at the deep stations, which can be attributed to stronger coupling at the shallow stations.

The sensor orientation estimated from the continuous data shows long-term temporal variations in the tilt and rotation angles. Figure 5 shows examples of stations N.S4N24 and N.S4N25. In addition to clear coseismic offsets, gradual long-term trends in tilt and rotation angles were evident. The long-term trends in rotation angle are greater than those in tilt angles.

Although the time series of sensor orientation contains such long-term trends, the total changes, defined by the difference between the maximum and minimum angles, do not exceed 1° for all the S-net stations during the time period from the beginning of 2017 to the end of 2018. At most stations, the total changes were within 10^{-3} to 10^{-1} degrees although they included coseismic changes. The stations shallower than 1500 m tended to have smaller total changes than those of the stations deeper than 1500 m. Reflecting this temporal stability, average information of tilt and rotation angles is provided in Ⓔ Table S1 (available in the supplemental content to this article), which could be sufficient for practical uses to obtain a three-component signal on a geographic coordinate system.

In addition to long-term trends, we observed temporal variations in the tilt and rotation angles. The mechanism of the temporal variations in the tilt and rotation angle was not determined but possibly results from combinations of change in sensor sensitivity because of temperature changes, ocean-bottom currents, and real seafloor deformation. Although it should be further examined, accelerometers might be a tool to detect and constrain the seafloor crustal deformation caused by tectonic events such as slow earthquakes, which have been found on the shallow plate interface off the Tohoku region and off the Boso Peninsula (e.g., Hirose *et al.* 2012; Uchida *et al.*, 2016; Ohta *et al.*, 2019; Tanaka *et al.*, 2019).

AZIMUTH

Data and Method

The gravitational acceleration on the DC components of the accelerometer does not provide a horizontal direction. Thus,

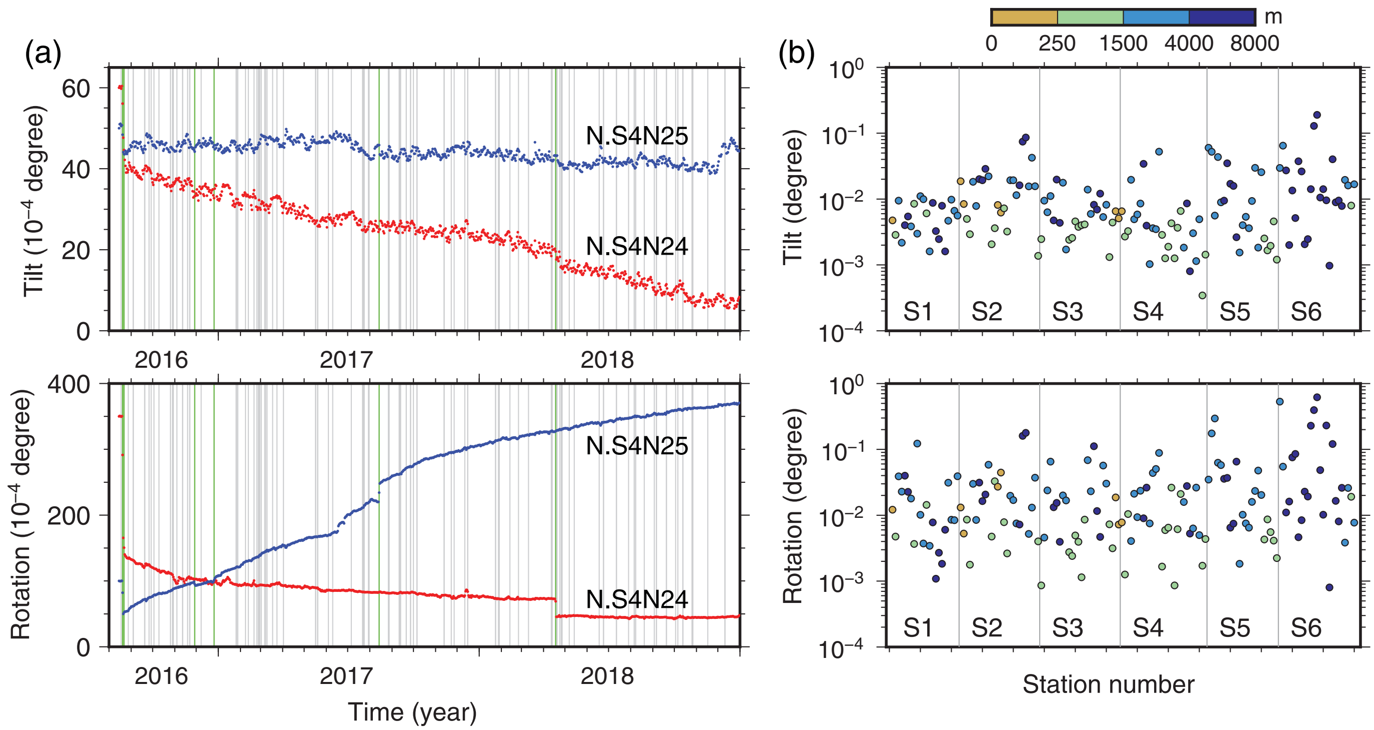

▲ **Figure 5.** (a) Examples of temporal variations in the tilt and rotation angles at N.S4N24 (red) and N.S4N25 (blue). The gray and green vertical bars show the dates with a PGA greater than 10^{-2} and 10^{-1}(m/s/s), respectively. (b) Difference between the maximum and minimum values of the tilt and rotation angles during the 2 yr time period of 2017 and 2018. The color shows the ocean depth at each station. The station number increases from left to right in each panel.

we estimated the azimuths of the sensors (the azimuth of the X component in the long axis of cable) using observed seismic waveforms. For longer period ranges more than a few seconds, the sensitivity of the strong-motion accelerometer is higher than that of the geophone (velocity sensor) because the natural frequency of the geophone is 15 Hz whereas the accelerometer has a flat response to the DC component. Therefore, we used seismograms observed by the strong-motion accelerometers. We used the vertical $a_U(t_i)$ and two horizontal waveforms $a_{X'}(t_i)$ and $a_{Y'}(t_i)$ by correcting the tilt and rotation angles based on the daily estimates of the tilt and rotation angles as follows:

$$\begin{pmatrix} a_{X'}(t_i) \\ a_{Y'}(t_i) \\ a_U(t_i) \end{pmatrix} = \begin{pmatrix} \cos\lambda & \sin\lambda\sin\theta & \sin\lambda\cos\theta \\ 0 & \cos\theta & -\sin\theta \\ -\sin\lambda & \cos\lambda\sin\theta & \cos\lambda\cos\theta \end{pmatrix} \begin{pmatrix} a_X(t_i) \\ a_Y(t_i) \\ a_Z(t_i) \end{pmatrix}, \tag{6}$$

in which $a_X(t_i)$, $a_Y(t_i)$, and $a_Z(t_i)$ are observed records in X, Y, and Z components, respectively.

We used the particle motion of teleseismic Rayleigh waves to estimate the sensor azimuths. Because fundamental-mode Rayleigh waves generally have retrograde motion on a plane parallel to the propagation direction, the polarization of the observed Rayleigh waves provides the propagation direction without the 180° ambiguity. When the Rayleigh wave propagates in the great circle path, we can estimate the azimuth of sensor from the geometry of the earthquake and station. Although the lateral variation in subsurface structure causes the ray path to move off the great circle, averaging the estimations with a wide back-azimuth range may reduce the effect of the off-great-circle paths. For anisotropic media, the Rayleigh-wave particle motion deviates from the plane parallel to the propagation direction (e.g., Maupin and Park, 2007). However, the possible biases are within the uncertainties of azimuth estimation because the deviation may be a few degrees for the anisotropy of the Pacific plate at less than 10% (Shimamura *et al.*, 1983; Shintaku *et al.*, 2014).

We used 14 teleseismic earthquakes of M_w 7.0–8.2 from 15 August 2016 to 31 December 2018 from the U.S. Geological Survey (USGS) earthquake catalog (Fig. 6; see Data and Resources). The focal depths of the earthquakes were shallower than 135 km, ensuring effective surface-wave excitation. The selected events cover a wide range of back azimuths. The frequency range for the analysis was 0.01–0.03 Hz. We selected the frequency range based on the signal-to-noise ratio of the surface waves. We used the time window satisfying $\Delta/v - 200(s) \le t \le \Delta/v + 400(s)$, in which Δ is the epicentral distance in km and v is the Rayleigh wavespeed. Here, v was set to 4.0 km/s.

For the elliptical Rayleigh wave, the vertical and radial waveforms have a 90° phase shift; thus, the vertical waveform

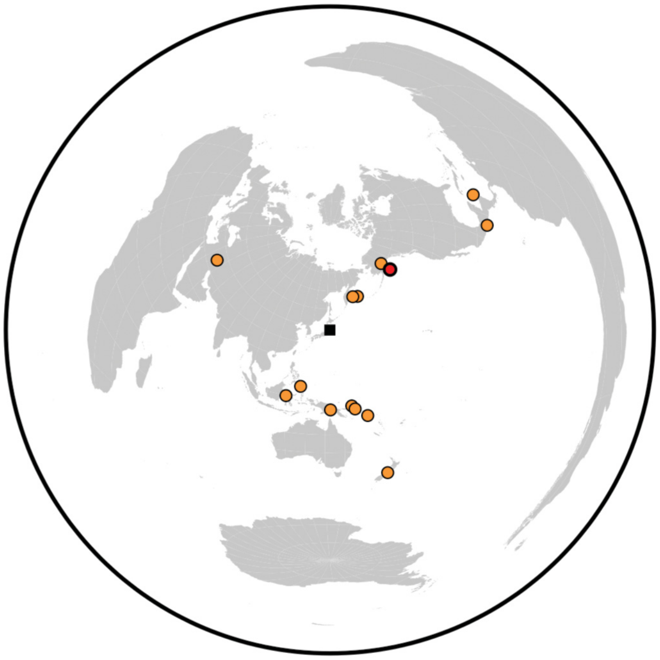

▲ **Figure 6.** Distribution of used teleseismic earthquakes. The orange circles show the teleseismic earthquakes, and the black square represents the location of S-net. The red circle is the 23 January 2018 M_w 7.9 Alaska earthquake, the waveforms of which are shown in Figures 8 and 9.

is a Hilbert transform of the radial waveform. We calculated cross-correlation coefficients between the Hilbert transformed vertical and radial waveforms by changing the sensor azimuth as follows:

$$\mathrm{cc}(\varphi) = \frac{\sum_{i=1}^{T}[-a_H(t_i)a_R(t_i, \varphi)]}{\sqrt{\sum_{i=1}^{T} a_H^2(t_i)}\sqrt{\sum_{i=1}^{T} a_R^2(t_i, \varphi)}}, \tag{7}$$

in which φ is the sensor azimuth (Fig. 2); $\mathrm{cc}(\varphi)$ is the cross-correlation coefficient; $a_H(t_i)$ and $a_R(t_i, \varphi)$ are the Hilbert transformed vertical waveform and radial waveform at time t_i, respectively; and T is the length of the time window. The sign of the numerator represents retrograde particle motion because the fundamental mode of long-period Rayleigh wave shows retrograde particle motion on the seafloor. The radial waveform $a_R(t_i, \varphi)$ is calculated as follows:

$$a_R(t_i, \varphi) = \cos(\varphi_p - \varphi)a_{X'}(t_i) + \sin(\varphi_p - \varphi)a_{Y'}(t_i), \tag{8}$$

in which $a_{X'}(t_i)$ and $a_{Y'}(t_i)$ are the two horizontal components after correction of the tilt and rotation angles defined by equation (6), and φ_p is the propagation azimuth of the Rayleigh wave, which is measured from east anticlockwisely.

The azimuth with the maximum correlation coefficient provides the sensor azimuth. We conducted the aforementioned procedure for all the teleseismic events and averaged the estimated sensor azimuths to obtain the best estimate and confidence intervals for the sensor azimuth. The average of the azimuths was calculated from the average of the unit vectors. We used the square of the maximum correlation coefficients as the weighting factor for the average. We only used data with maximum correlation coefficients greater than 0.7. We finally used 7–14 measurements for each station. The details of the estimation of the average azimuth and standard error are described in Appendix. Note that the standard error represents the standard deviation of the estimated value (i.e., average azimuth), not the standard deviation of the samples (i.e., azimuths from individual events).

Note that there are two means for the cross-correlation normalization (Baker and Stevens, 2004; Stachnik *et al.*, 2012). One is the typical cross-correlation coefficient using equation (7). The other normalizes the numerator of equation (7) with the square norm of the only vertical records as follows:

$$\mathrm{cc}(\varphi) = \frac{\sum_{i=1}^{T}[-a_H(t_i)a_R(t_i, \varphi)]}{\sum_{i=1}^{T} a_H^2(t_i)}. \tag{9}$$

We estimated the sensor azimuth based on both equations (7) and (9). The differences between the azimuths estimated from equations (7) and (9) were less than 5° for 85 stations, 10° for 135 stations, and 20° for all 150 stations. However, the average of the standard errors of the azimuth estimation from equation (9) was 1.8 times greater than that from equation (7). When the horizontal components consisted of only Rayleigh waves, the latter normalization greatly improved the azimuthal resolution because the denominator in equation (7) also changes with the azimuth φ. However, the time window used in the present study also included Love waves. In this case, normalization with only vertical records such as equation (9) may cause bias in the azimuth estimation because equation (9) contains amplitude information of the rotated horizontal waveform, which also depends on the amplitude ratio of Rayleigh and Love waves. Thus, we simply used the cross-correlation coefficient defined by equation (7).

Results and Discussion

Figures 1b and 7 show the difference between the estimated azimuths and the directions measured based on the cable route data (see Data and Resources). The cable route data are based on the ship trajectory, which are the sea surface locations where the cables were submerged, and provide rough directions of the long axis of the cables. The azimuthal differences from the cable route data are less than 10° at 136 and less than 24° at 148 out of the 150 stations. The general consistency between the estimated azimuth and the cable route data suggests that the orientation estimation method is reliable. The standard errors are 1.5°–6.2°. Thus, the 95% confidence intervals of the estimated sensor azimuths, which are estimated by two times of the standard errors, are ±3°–12° approximately. The estimated azimuths and standard errors are listed in Ⓔ Table S1.

Two stations show a large difference from the cable route data: N.S5N01 and N.S5N13. The azimuthal difference at N.S5N01 and N.S5N13 is −69° and 56°, respectively. Figure 8 shows the vertical and two radial waveforms: one radial

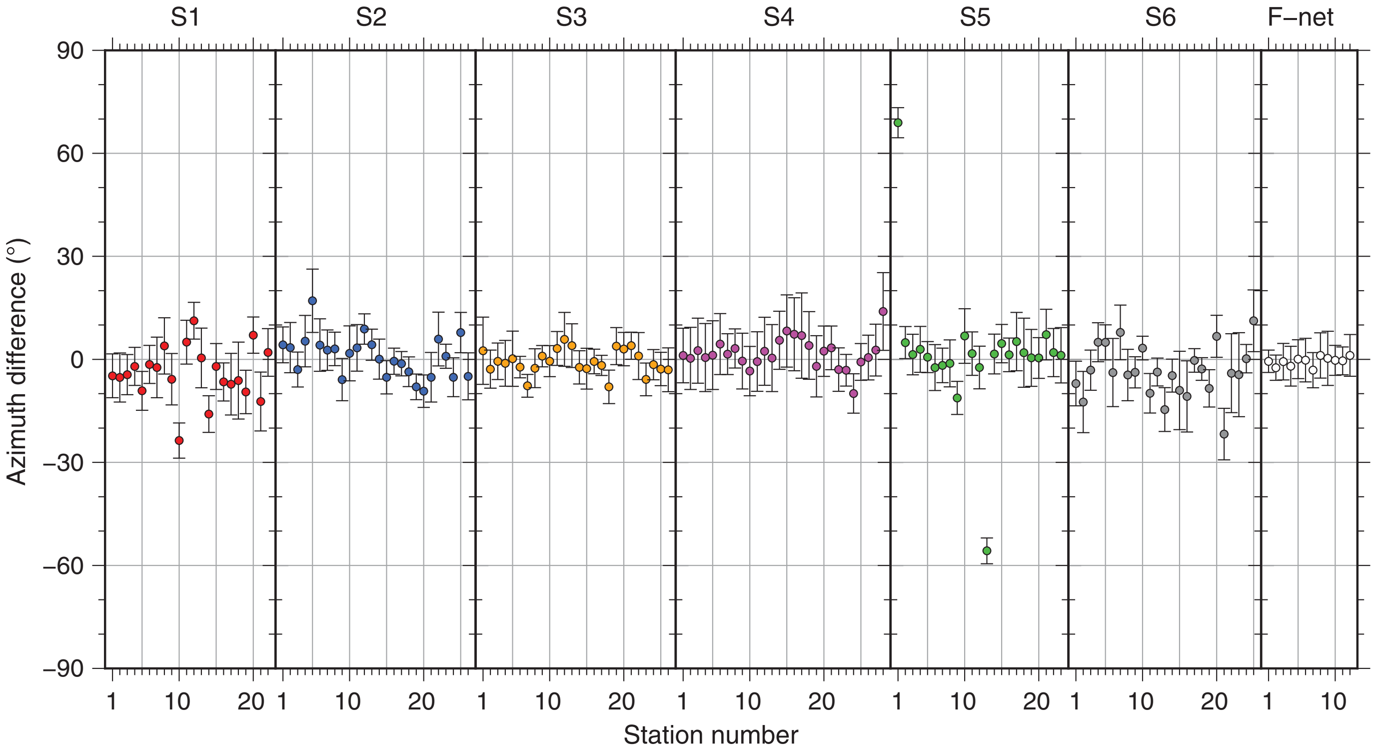

▲ **Figure 7.** Difference between the azimuth estimated by this study and the azimuth inferred from the cable route data. The open circles and error bars represent the mean values and their 95% confidence intervals. The S-net (S1–S6) and F-net (F) stations are shown in Figure 1a. The station number of F-net station shown in Figure 1a increases from north to south (i.e., 1 for station NMR and 12 for station TSK).

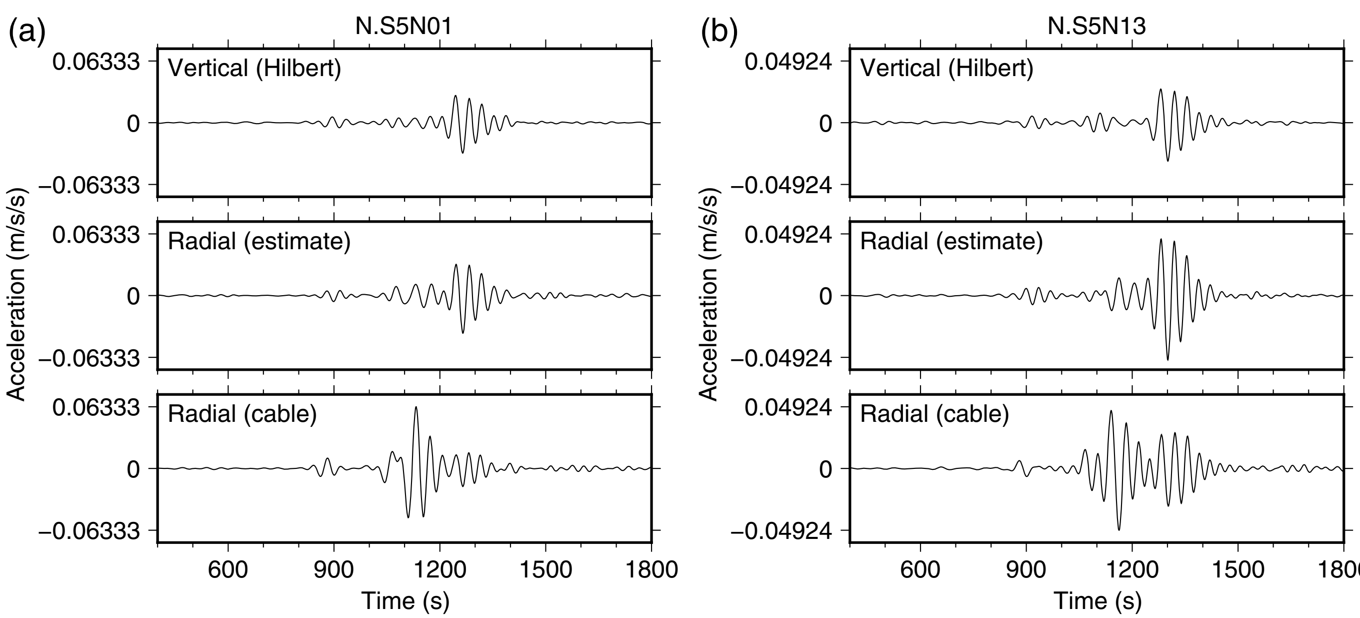

▲ **Figure 8.** Hilbert-transformed vertical and radial waveforms of the 2018 M_w 7.9 Alaska earthquake. We flipped the sign of the Hilbert-transformed vertical waveforms, considering retrograde particle motion. The time zero indicates the origin time. The frequency band is 0.01–0.03 Hz. (a) Waveforms at N.S5N01 and (b) waveforms at N.S5N13. The top, middle, and bottom panels show the Hilbert-transformed vertical waveform, radial waveform based on the estimated azimuth, and radial waveform based on the cable data, respectively.

waveform is based on the estimated azimuth and the other on the cable route data. The radial waveforms based on the estimated azimuth are more similar to the Hilbert-transformed vertical waveform than those based on the route cable data. The radial waveforms based on the cable data contain earlier Love waves caused by misorientation. Thus, we considered the estimated orientation is better than the cable route data.

Application of the same method to the F-net stations demonstrates the reliability of the sensor measurement because the sensor orientations of the surface F-net seismometers on land are accurately known (Fig. 7). The differences from the known orientations are less than 4° and the 95% confidence intervals include the true azimuth. This F-net station azimuthal consistency clearly shows that the azimuth estimation of this study is not strongly biased.

Note that several other methods have been used to estimate azimuths of seismic stations. They are based on the particle motion of P or T waves from earthquakes or airgun shots (e.g., Nakano *et al.*, 2012; Shan *et al.*, 2012; Tonegawa *et al.*, 2015; Tonegawa *et al.*, 2017), cross correlation between long-period seismograms of orientation-known and orientation-unknown stations (e.g., Shiomi *et al.*, 2003; Nakano *et al.*, 2012; Kano *et al.*, 2015), and ambient noise correlation (e.g., Zha *et al.*, 2013). The method based on airgun shots requires sufficient coverage of airgun shots for all S-net stations. Although we have tried the method based on the cross correlation between on-land seismic stations and S-net stations following Shiomi *et al.* (2003), the correlation coefficients were not sufficiently high to estimate reliable sensor azimuths. The low correlation coefficients may be attributed to the long distance between S-net and coastal on-land stations and to the difference in subsurface structure between the land and ocean. Ambient noise correlation may not be easy because the sensitivity of the sensors is low at the frequency ranges of microseisms and the sources of the microseisms are within the network (Takagi *et al.*, 2018).

The method based on *P*-wave particle motion may be the second candidate and a comparison to the results from Rayleigh-wave particle motions could improve reliability. Thus, we also estimated the sensor azimuth using *P*-wave particle motion following Nakano *et al.* (2012). We maximized the cross-correlation coefficient between the vertical and radial waveforms from 0.02 to 0.05 Hz with the normalization of equation (9). We used 100 second time windows from the theoretical *P*-wave travel time calculated using the IASP91 velocity model (Kennett and Engdahl, 1991). We averaged estimated azimuths over 2–8 teleseismic earthquakes of M_w 7.3–8.2 with high signal-to-noise ratio using the square of the cross-correlation coefficient as a weighting factor. The cross-correlation coefficient for the weighting factor was normalized in the manner of equation (7). We only used data with correlation coefficients greater than 0.7.

The estimated azimuths from the *P* waves were consistent with those from the Rayleigh waves (see Ⓔ Table S1 and Fig. S1). The differences between the azimuths estimated from the Rayleigh and *P*-wave particle motions were less than 5° for 96 stations, 10° for 133 stations, and 20° for all 150 stations. The average of the standard errors of the azimuth estimation from the *P*-wave particle motion was 1.4 times greater than that from the Rayleigh-wave particle motions. Thus, we treated the estimations from the Rayleigh waves as the main results.

DISCUSSION

We confirmed the orientation estimation using long-period teleseismic waveforms. Figure 9 shows the orientation-corrected record section of the teleseismic surface waves in 0.01–0.03 Hz at all the S-net stations. The surface-wave phases in the vertical component were spatially coherent at all S-net stations. They were also consistent with the seismograms of the on-land F-net stations. For the horizontal components, we converted the waveforms from the corrected east and north components to the radial and transverse components, respectively. The surface-wave phase in the horizontal components was also consistent within S-net itself and with F-net. Slower Rayleigh and faster Love waves were clearly separated into radial and transverse components, respectively. The record section clearly indicates that the estimated sensor orientations were well determined.

Converting XYZ to ENU components using the estimated parameters may be confusing because of the variety of angle definitions and inherent complexity of the 3D rotation. Thus, the rotation matrixes that convert XYZ to ENU components are more convenient for practical uses. Ⓔ Table S2 provides the rotation matrixes. Using the rotation matrixes, we simply obtain the ENU component records, $a_E(t_i)$, $a_N(t_i)$, and $a_U(t_i)$, from the XYZ component records, $a_X(t_i)$, $a_Y(t_i)$, and $a_Z(t_i)$, as follows:

$$\begin{pmatrix} a_E(t_i) \\ a_N(t_i) \\ a_U(t_i) \end{pmatrix} = \begin{pmatrix} R_{11} & R_{12} & R_{13} \\ R_{21} & R_{22} & R_{23} \\ R_{31} & R_{32} & R_{33} \end{pmatrix} \begin{pmatrix} a_X(t_i) \\ a_Y(t_i) \\ a_Z(t_i) \end{pmatrix}. \tag{10}$$

Here, we used the average of the tilt and rotation angles from 2017 to 2018 because they were stable within 0.001°–0.1° at most stations. When the precise tilt and rotation angles were needed or they changed largely because of strong motions, we may revise the rotation matrix as follows:

$$\mathbf{R} = \begin{pmatrix} R_{11} & R_{12} & R_{13} \\ R_{21} & R_{22} & R_{23} \\ R_{31} & R_{32} & R_{33} \end{pmatrix} = \begin{pmatrix} \cos\varphi\cos\lambda & \cos\varphi\sin\lambda\sin\theta - \sin\varphi\cos\theta & \cos\varphi\sin\lambda\cos\theta + \sin\varphi\sin\theta \\ \sin\varphi\cos\lambda & \sin\varphi\sin\lambda\sin\theta + \cos\varphi\cos\theta & \sin\varphi\sin\lambda\cos\theta - \cos\varphi\sin\theta \\ -\sin\lambda & \cos\lambda\sin\theta & \cos\lambda\cos\theta \end{pmatrix}, \tag{11}$$

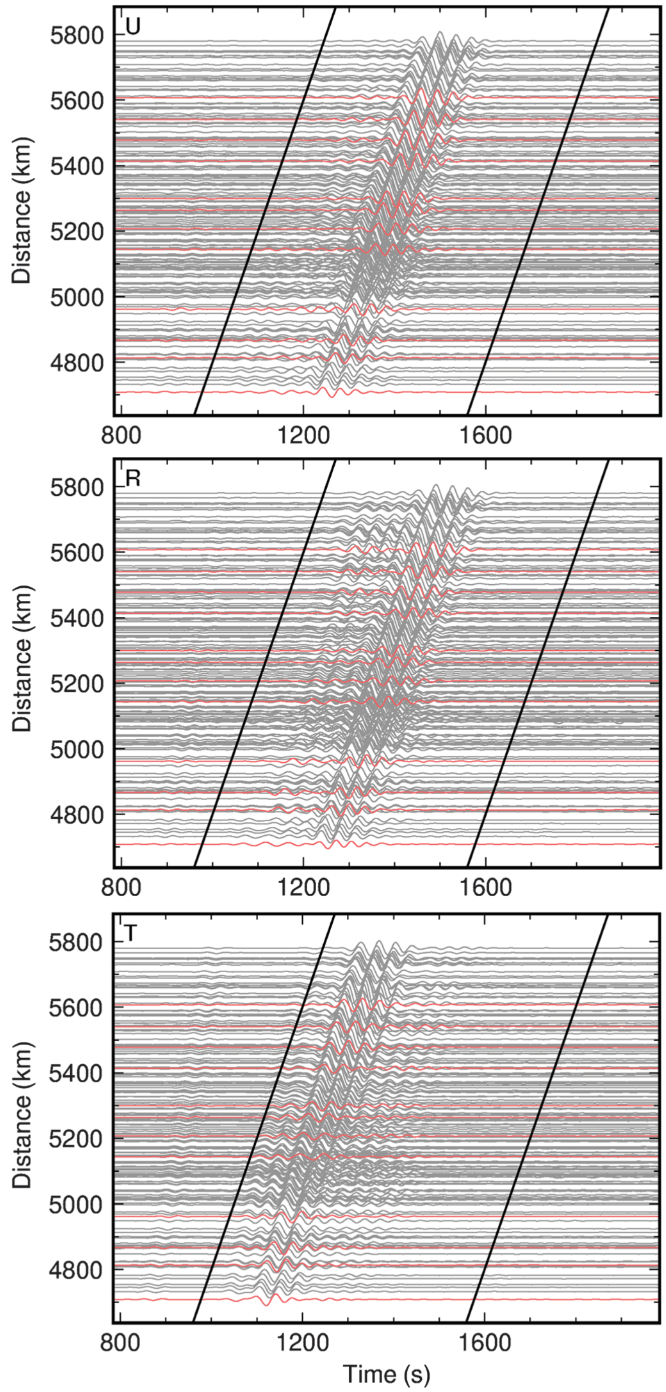

▲ **Figure 9.** Teleseismic waveforms of the 2018 M_w 7.9 Alaska earthquake in the frequency range of 0.01–0.03 Hz. The horizontal axis represents the lapse time from the origin of the earthquake. Up (U), radial (R), and transverse (T) component waveforms were converted from the XYZ component waveforms based on the estimated sensor orientations. The gray and red curves represent the waveforms at the S-net and F-net stations, respectively. The two inclined lines show the time window used to estimate the sensor azimuths.

in which φ, λ, and θ are azimuth (yaw), tilt (pitch), and rotation (roll) angles, respectively, in the definition of Figure 2.

The orientation information should expand the range of data analysis: selecting first-motion polarity for focal mechanism estimation, centroid moment tensor analysis based on waveform fitting, shear-wave splitting analysis, receiver function analysis, three-component ambient noise correlation analysis, seismic gradiometry, and so on. The present work provides fundamental information and an essential resource for the frontier research field provided by the NIED S-net.

CONCLUSIONS

We estimated the sensor orientations of S-net. The tilt and rotation angles were estimated from the DC offsets in the accelerometer records. Although the tilt and rotation angles show coseismic changes because of strong ground motion, coseismic changes greater than 1° were observed only during two earthquakes in 2016. The tilt and rotation angles were temporally stable within the range of 0.001°–0.1° for most stations and did not exceed 1° from 2017 to 2018. The sensor azimuths were estimated from polarization of the teleseismic long-period Rayleigh waves. They were determined with 95% confidence intervals of ±3°–12°. Waveforms converted using the estimated sensor orientation showed the spatial coherency of the wave phase for all S-net stations and consistency with the on-land F-net stations. We provided the estimated sensor orientations and rotation matrix for converting XYZ to ENU components. The information provided by the present study can serve as a fundamental resource for further seismic and geodetic data analysis using S-net.

DATA AND RESOURCES

The S-net and F-net continuous waveform data are available from http://www.hinet.bosai.go.jp/. The S-net cable route data are available from http://www.seafloor.bosai.go.jp/st_info_map/. The Japan Meteorological Agency (JMA) unified earthquake catalog is available from https://www.data.jma.go.jp/svd/eqev/data/bulletin/index_e.html and https://www.data.jma.go.jp/svd/eqev/data/daily_map/index.html. The U.S. Geological Survey (USGS) earthquake catalog is available from https://earthquake.usgs.gov/earthquakes/search/. Some plots were developed using Generic Mapping Tools v.5.4.3 (http://gmt.soest.hawaii.edu; Wessel *et al.*, 2013). All the websites were last accessed during April 2019.

ACKNOWLEDGMENTS

The authors sincerely appreciate National Research Institute for Earth Science and Disaster Resilience (NIED) for developing and managing S-net and F-net and for providing continuous records. Discussions with Akira Hasegawa, Ryota Hino, Tatsuya Kubota, Toru Matsuzawa, Genti Toyokuni, and Tatsuhiko Saito were helpful. R. T. was funded by Japan Society for the Promotion of Science (JSPS) Grants-in-Aid for Scientific

Research Program Grant Numbers JP16H06474, JP17H02950, and 19K14809. N. U. was funded by JSPS Grants-in-Aid for Scientific Research Program Grant Numbers 15K05260, JP16H06473, and 17H05309. This study was also supported by the Ministry of Education, Culture, Sports, Science and Technology of Japan, under its Earthquake and Volcano Hazards Observation and Research Program. The authors thank Editor-in-Chief Zhigang Peng, an Associate Editor, and an anonymous reviewer for their thoughtful reviews of the article.

REFERENCES

Aoi, S. (2016). Operation and current status of Seafloor Observation Network for Earthquakes and Tsunamis along the Japan Trench (S-net) (in Japanese), presented at *77th Subcommittee for Survey and Observation Planning, the Policy Committee of the Headquarters for Earthquake Research Promotion of Japanese Government*, Tokyo, Japan, 8 July, https://www.jishin.go.jp/main/seisaku/hokoku16g/k77-2.pdf (last accessed April 2019).

Arai, H. (2011). Circular statistics for the analysis of directional geological data (in Japanese with English abstract), *J. Geol. Soc. Japan* **117,** no. 10, 547–564, doi: 10.5575/geosoc.117.547.

Baker, G. E., and J. L. Stevens (2004). Back azimuth estimation reliability using surface wave polarization, *Geophys. Res. Lett.* **31,** L09611, doi: 10.1029/2004GL019510.

Best, D. J., and N. I. Fisher (1981). The bias of the maximum likelihood estimators of the von mises-fisher concentration parameters, *Commun. Stat. Simul. Comput.* **10,** no. 5, 493–502, doi: 10.1080/03610918108812225.

Davis, J.C. (2002). *Statistics and Data Analysis in Geology*, Third Ed., John Wiley & Sons, Inc., New York, New York, 316–331.

Hasegawa, A., N. Umino, and A. Takagi (1978). Double-planed deep seismic zone and upper-mantle structure in the northeastern Japan Arc, *Geophys. J. R. Astr. Soc.* **54,** 281–296, doi: 10.1111/j.1365-246X.1978.tb04260.x.

Hirose, H., H. Kimura, B. Enescu, and S. Aoi (2012). Recurrent slow slip event likely hastened by the 2011 Tohoku earthquake, *Proc. Natl. Acad. Sci. Unit. States Am.* **109,** no. 38, 15,157–15,161, doi: 10.1073/pnas.1202709109.

Kanazawa, T. (2013). Japan Trench earthquake and tsunami monitoring network of cable-linked 150 ocean bottom observatories and its impact to earth disaster science (UT2013-1147), presented at *2013 IEEE International Symposium on Underwater Technology*, Tokyo, Japan, 5–8 March, doi: 10.1109/UT.2013.6519911.

Kanazawa, T., K. Uehira, M. Mochizuki, T. Shinbo, H. Fujimoto, S. Noguchi, T. Kunugi, K. Shiomi, S. Aoi, T. Matsumoto, S. Sekiguchi, and Y. Okada (2016). S-net project, cable observation network for earthquakes and tsunamis, presented at *SubOptic 2016 Proceedings WE2B3*, Dubai, 18–21 April, https://suboptic.org/suboptic-2016/ (last accessed April 2019).

Kano, M., H. Nagao, S. Sakai, S. Nakagawa, S. Mizusako, M. Hori, N. Hirata, K. Shiomi, and R. Honda (2015). Azimuth verification of the MeSO-net seismographs (in Japanese with English abstract), *Zisin* **68,** 31–44, doi: 10.4294/zisin.68.31.

Kennett, B. L. N., and E. R. Engdahl (1991). Travel times for global earthquake location and phase identification, *Geophys. J. Int.* **105,** 429–465, doi: 10.17611/DP/9991809.

Maupin, V., and J. Park (2007). Theory and observations—Wave propagation in anisotropic media, in *Treatise on Geophysics, Vol. 1, Seismology and the Structure of the Earth*, B. Romanowicz and A. Dziewonski (Editors), Elsevier, Boston, Massachusetts, 289–321, doi: 10.1016/B978-044452748-6.00007-9.

Mochizuki, M., T. Kanazawa, K. Uehira, T. Shinbo, K. Shiomi, T. Kunugi, S. Aoi, T. Matsumoto, S. Sekiguchi, N. Yamamoto, *et al.* (2016). S-net project: Construction of large scale seafloor observatory network for tsunamis and earthquakes in Japan, presented at *2016 AGU Fall Meeting*, San Francisco, California, December
12–16, Abstract NH43B–1840.

Nakamura, T., and N. Hayashimoto (2019). Rotation motions of cabled ocean-bottom seismic stations during the 2011 Tohoku earthquake and their effects on magnitude estimation for early warnings, *Geophys. J. Int.* **216,** 1413–1427, doi: 10.1093/gji/ggy502.

Nakano, M., T. Tonegawa, and Y. Kaneda (2012). Orientations of DONET seismometers estimated from seismic waveforms, *JAMSTEC Rep. Res. Dev.* **15,** 77–89, doi: 10.5918/jamstecr.15.77.

National Research Institute for Earth Science and Disaster Resilience (2019a). *NIED F-net*, National Research Institute for Earth Science and Disaster Resilience, doi: 10.17598/NIED.0005.

National Research Institute for Earth Science and Disaster Resilience (2019b). *NIED S-net*, National Research Institute for Earth Science and Disaster Resilience, doi: 10.17598/NIED.0007.

Ohta, K., Y. Ito, R. Hino, S. Ohyanagi, T. Matsuzawa, H. Shiobara, and M. Shinohara (2019). Tremor and inferred slow slip associated with afterslip of the 2011 Tohoku earthquake, *Geophys. Res. Lett.* **46,** 4591–4598, doi: 10.1029/2019GL082468.

Shan, S., H. Kao, and K. Obana (2012). Structural characteristics of the northern Cascadia deformation front: Preliminary result of SeaJade Experiment, presented at *2012 AGU Fall Meeting*, San Francisco, California, 3–7 December, Abstract T22D–04.

Shimamura, H., T. Asada, K. Suyehiro, T. Yamada, and H. Inatani (1983). Longshot experiments to study velocity anisotropy in the oceanic lithosphere of the northwestern Pacific, *Phys. Earth Planet. Int.* **31,** 348–362, doi: 10.1016/0031-9201(83)90094-8.

Shintaku, N., D. W. Forsyth, C. J. Hajewski, and D. S. Weeraratne (2014). *Pn* anisotropy in Mesozoic western Pacific lithosphere, *J. Geophys. Res.* **119,** 3050–3063, doi: 10.1002/2013JB010534.

Shiomi, K., K. Obara, S. Aoi, and K. Kasahara (2003). Estimation on the azimuth of the Hi-net and KiK-net borehole seismometers (in Japanese with English abstract), *Zisin* **56,** 99–110, doi: 10.4294/zisin1948.56.1_99.

Stachnik, J. C., A. F. Sheehan, D. W. Zietlow, Z. Yang, J. Collins, and A. Ferris (2012). Determination of New Zealand ocean bottom seismometer orientation via Rayleigh-wave polarization, *Seismol. Res. Lett.* **83,** 704–713, doi: 10.1785/0220110128.

Takagi, R., K. Nishida, T. Maeda, and K. Obara (2018). Ambient seismic noise wavefield in Japan characterized by polarization analysis of Hi-net records, *Geophys. J. Int.* **215,** 1682–1699, doi: 10.1093/gji/ggy334.

Tanaka, S., T. Matsuzawa, and Y. Asano (2019). Shallow low-frequency tremor in the northern Japan Trench subduction zone, *Geophys. Res. Lett.* **46,** 5217–5224, doi: 10.1029/2019GL082817.

Tonegawa, T., Y. Fukao, G. Fujie, S. Takemura, T. Takahashi, and S. Kodaira (2015). Geographical distribution of shear wave anisotropy within marine sediments in the northwestern Pacific, *Prog. Earth Planet. Sci.* **2,** 27, doi: 10.1186/s40645-015-0057-2.

Tonegawa, T., K. Obana, Y. Yamamoto, S. Kodaira, K. Wang, M. Riedel, H. Kao, and G. Spence (2017). Fracture alignments in marine sediments off Vancouver Island from Ps splitting analysis, *Bull. Seismol. Soc. Am.* **107,** no. 1, 387–402, doi: 10.1785/0120160090.

Uchida, N., T. Iinuma, R. M. Nadeau, R. Bürgmann, and R. Hino (2016). Periodic slow slip triggers megathrust zone earthquakes in northeastern Japan, *Science* **351,** 488–492, doi: 10.1126/science.aad3108.

Uehira, K., T. Kanazawa, M. Mochizuki, H. Fujimoto, S. Noguchi, T. Shinbo, K. Shiomi, T. Kunugi, S. Aoi, T. Matsumoto, *et al.* (2016). Outline of Seafloor Observation Network for Earthquakes and Tsunamis along the Japan Trench (S-net), presented at *European Geosciences Union General Assembly 2016*, Vienna, Austria, 17–22 April, Abstract EGU2016–13832.

Wessel, P., W. H. F. Smith, R. Scharroo, J. F. Luis, and F. Wobbe (2013). Generic mapping tools: Improved version released, *Eos Trans. AGU* **94,** 409–410, doi: 10.1002/2013EO450001.

Zha, Y., S. C. Webb, and W. Menke (2013). Determining the orientations of ocean bottom seismometers using ambient noise correlation, *Geophys. Res. Lett.* **40,** 3585–3590, doi: 10.1002/grl.50698.

APPENDIX

The average sensor azimuths $\hat{\varphi}$ are estimated by

$$\hat{\varphi} = \arctan\left(\frac{\bar{v}_y}{\bar{v}_x}\right), \tag{A1}$$

in which $\bar{v}_x$ and $\bar{v}_y$ represent the weighted average of the unit vectors as

$$\bar{v}_x = \frac{\sum_{i=1}^{N} w_i \cos\varphi_i}{\sum_{i=1}^{N} w_i}, \bar{v}_y = \frac{\sum_{i=1}^{N} w_i \sin\varphi_i}{\sum_{i=1}^{N} w_i}. \tag{A2}$$

φ_i is the azimuth with the maximum correlation coefficient estimated from ith earthquake, w_i is the square of the maximum correlation coefficient, and N is the number of earthquakes used.

We estimated the standard error of the sensor azimuth $\sigma_{\hat{\varphi}}$ in two ways. The first estimation is based on the error propagation from the standard errors of the average of the unit vectors $\sigma_{\bar{v}_x}$ and $\sigma_{\bar{v}_y}$ as follows:

$$\sigma_{\hat{\varphi}} = \sqrt{\frac{\bar{v}_y^2 \sigma_{\bar{v}_x}^2 + \bar{v}_x^2 \sigma_{\bar{v}_y}^2}{(\bar{v}_x^2 + \bar{v}_y^2)^2}}, \tag{A3}$$

where

$$\sigma_{\bar{v}_x} = \sqrt{\frac{\sum_{i=1}^{N} w_i (\cos\varphi_i - \bar{v}_x)^2}{(N-1)\sum_{i=1}^{N} w_i}}, \sigma_{\bar{v}_y} = \sqrt{\frac{\sum_{i=1}^{N} w_i (\sin\varphi_i - \bar{v}_y)^2}{(N-1)\sum_{i=1}^{N} w_i}}. \tag{A4}$$

Note that $\sigma_{\bar{v}_x}$ and $\sigma_{\bar{v}_y}$ are not the standard deviations of $\cos\varphi_i$ and $\sin\varphi_i$, respectively, but the standard deviations of $\bar{v}_x$ and $\bar{v}_y$ (i.e., standard errors), respectively.

The second estimation is based on the circular statistics (e.g., Arai, 2011; Davis, 2002). The standard error of the mean azimuth can be estimated by

$$\sigma_{\hat{\varphi}} = \frac{1}{\sqrt{N\bar{R}\kappa}}, \tag{A5}$$

in which $\bar{R}$ is the length of the average of the unit vectors as

$$\bar{R} = \sqrt{\bar{v}_x^2 + \bar{v}_y^2}, \tag{A6}$$

and κ is the concentration parameter of the von Mises distribution, which is a standard probability distribution for circular data. κ is estimated from $\bar{R}$ according to an approximate expression of Best and Fisher (1981).

The difference between the two estimations of the standard errors for the average sensor azimuth estimated from Rayleigh waves is 0.1° on average and 1.4° at the maximum. Because the estimations of equation (A3) tend to be larger than those of equation (A5), we mainly described the error of azimuth based on equation (A3) and only show the estimations by equation (A5) as a reference in Ⓔ Table S1.

Ryota Takagi
Naoki Uchida
Takashi Nakayama
Ryosuke Azuma
Akira Ishigami
Tomomi Okada
Research Center for Prediction of Earthquakes and Volcanic Eruptions
Graduate School of Science
Tohoku University
6-6 Aza-Aoba, Aramaki, Aoba-ku
Sendai 980-8578, Japan
ryota.takagi.c1@tohoku.ac.jp
naoki.uchida.b6@tohoku.ac.jp
takashi.nakayama.c8@tohoku.ac.jp
ryosuke.azuma.c8@tohoku.ac.jp
akira.ishigami.p3@dc.tohoku.ac.jp
tomomi.okada.a4@tohoku.ac.jp

Takeshi Nakamura
Katsuhiko Shiomi
National Research Institute for Earth Science and Disaster Resilience
3-1 Tennodai, Tsukuba
Ibaraki 305-0006, Japan
t_nakamura@bosai.go.jp
shiomi@bosai.go.jp

Published Online 11 September 2019